BIOCHEMISTRY
including biophysical chemistry & molecular biology

Article

pubs.acs.org/biochemistry

The Selectivity of *Vibrio cholerae* H-NOX for Gaseous Ligands Follows the "Sliding Scale Rule" Hypothesis. Ligand Interactions with both Ferrous and Ferric *Vc* H-NOX

Gang Wu,* Wen Liu, Vladimir Berka, and Ah-lim Tsai*

Division of Hematology, Department of Internal Medicine, The University of Texas-Medical School at Houston, 6431 Fannin Street, Houston, Texas 77030, United States

Supporting Information

ABSTRACT: *Vc* H-NOX (or VCA0720) is an H-NOX (heme-nitric oxide and oxygen binding) protein from facultative aerobic bacterium *Vibrio cholerae*. It shares significant sequence homology with soluble guanylyl cyclase (sGC), a NO sensor protein commonly found in animals. Similar to sGC, *Vc* H-NOX binds strongly to NO and CO with affinities of 0.27 nM and 0.77 μM, respectively, but weakly to O_2. When positioned on a "sliding scale" plot [Tsai, A.-l., et al. (2012) *Biochemistry 51*, 172−186], the line connecting log K_D(NO) and log K_D(CO) of *Vc* H-NOX can almost be superimposed with that of *Ns* H-NOX. Therefore, the measured affinities and kinetic parameters of gaseous ligands to *Vc* H-NOX provide more evidence to validate the "sliding scale rule" hypothesis. Like sGC, *Vc* H-NOX binds NO in multiple steps, forming first a six-coordinate heme−NO complex at a rate of 1.1 × 10^9 M^{-1} s^{-1}, and then converts to a five-coordinate heme−NO complex at a rate that is also dependent on NO concentration. Although the formation of oxyferrous *Vc* H-NOX cannot be detected at a normal atmospheric oxygen level, ferrous *Vc* H-NOX is oxidized to the ferric form at a rate of 0.06 s^{-1} when mixed with O_2. Ferric *Vc* H-NOX exists as a mixture of high- and low-spin states and is influenced by binding to different ligands. Characterization of both ferric and ferrous *Vc* H-NOX and their complexes with various ligands lays the foundation for understanding the possible dual roles in gas and redox sensing of *Vc* H-NOX.

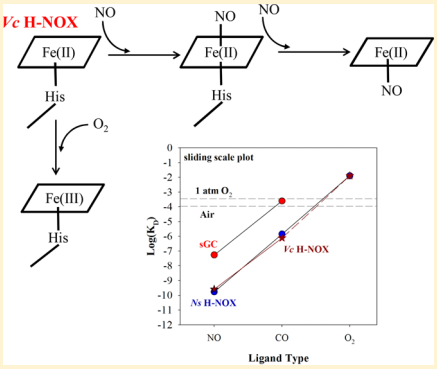

Heme sensor proteins exhibit selective reversible binding of diatomic gaseous molecules, including CO, NO, and O_2, and play important roles in physiological inter- and intracellular signaling.[1−4] The selectivity of heme sensor proteins in association with these small gaseous molecules is determined by several factors, including the type of proximal ligand, direct distal steric hindrance, proximal constraints for in-plane iron movement, the presence of a distal site hydrogen bond donor, and multiple steps in association with NO.[3] A 3−4 order of magnitude increase from K_D(NO) to K_D(CO) to K_D(O_2), regardless of the absolute value of each individual K_D, is observed for many five-coordinate (5c) ferrous hemoproteins and protoporphyrin IX(1-methylimidazole) [PP(1-MeIm)] heme model with a neutral imidazole proximal ligand but lacking a distal hydrogen bond donor. The log K_D(NO), log K_D(CO), and log K_D(O_2) values of each of these hemoproteins and heme model PP(1-MeIm) fall on an approximately straight line when they are plotted versus gaseous ligand type, and these lines approximately parallel one another and span a vertical range of 9 orders of magnitude, which has recently prompted the coining of the phrase "sliding scale rule".[5] If such a hypothesis is proven to be valid with a large database, it will establish a paradigm for the gaseous ligand selectivity by a plethora of heme-based sensors. Thus, the K_D measured for one gaseous ligand can be used to predict the affinities of the other two gaseous ligands via the parallel relationship with that of the heme model. The validity of the sliding scale rule hypothesis has been checked against more than 100 hemoproteins, mutants, and model compounds; however, to validate this hypothesis as a general rule, it is necessary to characterize the binding of gaseous ligands for additional heme sensor proteins to provide statistical support.

Soluble guanylyl cyclase (sGC), the only authentic NO receptor found in mammalian systems, catalyzes the conversion of GTP to cGMP.[6] sGC is a heterodimer containing α and β subunits, and the ferrous heme in the β subunit exhibits a strong affinity for NO but no binding with O_2.[6,7] NO binds to sGC to form a six-coordinate (6c) NO−heme−His complex with subsequent conversion to a 5c NO−heme complex and stimulates its guanylate cyclase activity by several hundred-fold.[8,9] The affinities of NO and CO for sGC to form the 6c complexes are 54 nM and 260 μM, respectively, being positioned well on the "sliding scale" plot.[5] On the basis of the affinities of NO and CO for sGC, the K_D(O_2) of sGC is predicted to be well above oxygen concentration in aqueous

Received: October 14, 2013
Revised: December 10, 2013
Published: December 10, 2013

   dx.doi.org/10.1021/bi401408x | *Biochemistry* 2013, 52, 9432−9446

solution, ~260 μM at 24 °C, thus explaining the total exclusion of O_2 binding from sGC.[5]

sGC belongs to the H-NOX (heme-nitric oxide and oxygen binding) or SONO (sensor of NO)[10] family of heme sensor proteins found in both prokaryotic and eukaryotic organisms.[7] H-NOX proteins exhibit a high degree of homology in sequence and structure to the β subunit of sGC and selectively bind NO or O_2 based on the immediate structure of their heme pockets.[2,3,7,11] A subgroup of H-NOX proteins, exemplified by the heme domain of a methyl-accepting chemotaxis protein from *Thermoanaerobacter tengcongensis*, binds O_2 with high affinity.[12] This is due to the existence of a hydrogen bond donor, Tyr140, in its heme distal pocket, leading to selectively enhanced binding of O_2.[7,13] Other H-NOX proteins, including eukaryotic sGC and a prokaryotic H-NOX from *Nostoc punctiforme* (*Ns* H-NOX), have hydrophobic distal heme pockets without any hydrogen bonding donor.[9,14] The characteristics of gaseous ligand binding to *Ns* H-NOX, which is 33% identical in sequence with the β subunit of human sGC, are similar to those of sGC.[14] Ferrous *Ns* H-NOX binds NO and CO with K_D values of 0.17 nM and 1.4 μM, respectively, and the line connecting the two values of log K_D parallels that of sGC on the sliding scale plot.[5] On the basis of its affinity for NO being stronger than that of sGC, its K_D for O_2 is expected to be lower than that of sGC and is actually measured to be 13 mM using a high-pressure cell.[5] This O_2 concentration is still much higher than that available at atmospheric pressure, and therefore, Fe(II) *Ns* H-NOX does not exhibit appreciable O_2 binding either.

Another H-NOX protein identified from the genome of a facultative aerobic bacterium *Vibrio cholerae*, *Vc* H-NOX (also called VCA0720), is a protein of 181 amino acids and has a sequence that is 22% identical to that of the rat sGC β1 subunit (residues 1−194).[12] Initial spectroscopic studies indicate that Fe(II) *Vc* H-NOX selectively binds NO and CO but shows no binding to O_2, similar to sGC and *Ns* H-NOX.[12] Resonance Raman spectroscopy indicates that Fe(II) *Vc* H-NOX exists in a high-spin state.[12] Ferrous *Vc* H-NOX binds CO readily to form a 6c heme−CO complex and NO to form a 5c heme−NO complex in the presence of an excess of NO.[12] Information about K_D values and the kinetics of binding of NO and CO to *Vc* H-NOX, however, is lacking. Moreover, it is unknown whether NO binds to *Vc* H-NOX in multiple steps, as observed in some H-NOX proteins like sGC and *Ns* H-NOX.[8,14]

In this study, we determined the binding affinities and the kinetics of gaseous ligands to Fe(II) *Vc* H-NOX and checked the validity of the sliding scale rule hypothesis using the measured parameters. Our results demonstrate that the binding of NO and the binding of CO to Fe(II) *Vc* H-NOX are consistent with the sliding scale rule hypothesis, which also nicely explains why O_2 does not bind to Fe(II) *Vc* H-NOX. NO is found to bind Fe(II) *Vc* H-NOX in multiple steps. Some differences were observed between the binding kinetics of NO and O_2 with respect to *Vc* H-NOX and with respect to sGC and *Ns* H-NOX. We also studied the heme geometry in ferric *Vc* H-NOX and its complexes with ligands using magnetic circular dichroism (MCD) and electron paramagnetic resonance (EPR). This study provides new information about the possible signaling pathways for this human pathogen to respond to the environmental NO level and the redox states and therefore should provide insight into the virulence of this human pathogen mediated via either the ferrous or ferric state of the heme.

MATERIALS AND METHODS

Materials. Carbon monoxide (CO) and nitric oxide (NO) gases were from Matheson-TriGas Inc. (Houston, TX). NO was prepurified by being passed through a NaOH trap to remove nitrous and nitric acid contaminants. Sodium ferricyanide, sodium hydrosulfite (85%), sodium fluoride, sodium azide, sodium cyanide, imidazole, δ-aminolevulinic acid, and isopropyl 1-thio-β-D-galactopyranoside were from Sigma (St. Louis, MO). A cyanide stock solution (1 M, pH ~9) was prepared by titration of a water solution of sodium cyanide with HCl at 0 °C. Other chemicals were all of reagent grade.

Construction of the Expression Vector for His-Tagged *Vc* H-NOX. The gene sequence of *Vc* H-NOX (GenBank entry 15601476) was first optimized for *Escherichia coli* codon usage, replacing several rare codons with high-frequency synonymous codons to form a synthetic gene encoding *Vc* H-NOX. Six histidine codons were then inserted upstream of the stop codon, and *Vc* H-NOX cDNA was synthesized and cloned into the pBSK vector (Epoch LifeScience, Houston, TX). The cDNA was released by digestion with *Nde*I and *Xho*I and subcloned into pET43.1a (predigested with *Nde*I and *Xho*I). The integrity of the resulting plasmid was confirmed by restriction digestion and DNA sequencing (Lone Star Laboratories, Houston, TX).

Expression and Purification of *Vc* H-NOX. The Rosetta 2(DE3)pLysS *E. coli* strain (Novagen, Madison, WI) was transformed with the pET43.1a *Vc* H-NOX expression plasmid and grown overnight in Terrific Broth containing chloramphenicol (45 μg/mL) and ampicillin (150 μg/mL) at 37 °C. The overnight culture was used to inoculate Terrifc Broth containing ampicillin (150 μg/mL) and incubated while being shaken (200 rpm) at 37 °C until the A_{610} reached 0.8. After the mixture had been cooled to 20 °C, heme (2 μM), δ-aminolevulinic acid (0.2 mM), and isopropyl 1-thio-β-D-galactopyranoside (1 mM) were added, and the culture was shaken for 48 h at 20 °C. Cells were harvested by centrifugation.

To purify *Vc* H-NOX, cells were resuspended in 100 mM potassium phosphate (pH 7.5) containing 100 mM NaCl, 10% glycerol, and egg lysozyme (1 mg/mL). The suspension was stirred at 4 °C, sonicated, and then centrifuged at 100000 *g*. The supernatant containing recombinant *Vc* H-NOX was then mixed with TALON affinity resin (Clontech Laboratories, Mountain View, CA). *Vc* H-NOX was eluted with the same buffer containing 250 mM imidazole, which was later removed using 10 DG desalting columns.

The purity of the purified *Vc* H-NOX was checked via 12% sodium dodecyl sulfate−polyacrylamide gel electrophoresis (SDS−PAGE) and Coomassie blue staining. The amount of protein was determined with a Bio-Rad (Hercules, CA) kit using bovine serum albumin as the standard. The heme content was determined by the pyridine hemochrome method based on the relation $A_{556} - A_{538} = 24.5\ mM^{-1}\ cm^{-1}$.

Electronic Absorption and Magnetic Circular Dichroism (MCD). Electronic absorption spectra were recorded using a Hewlett-Packard 8452A diode-array spectrophotometer with an optical resolution of 2 nm. MCD spectra in the UV−vis region were recorded with a Jasco (Tokyo, Japan) J-815 CD spectrometer. The magnetic field was provided with an Olis (Bogart, GA) magnet, and the field strength was calibrated with a ferricyanide solution using a ΔA_{420} of 3.0 $M^{-1}\ cm^{-1}\ T^{-1}$. Experiments were conducted at room temperature at a

dx.doi.org/10.1021/bi401408x | *Biochemistry* 2013, 52, 9432−9446

Scheme 1. Binding of Gaseous Ligands to Fe(II) *Vc* H-NOX[a]

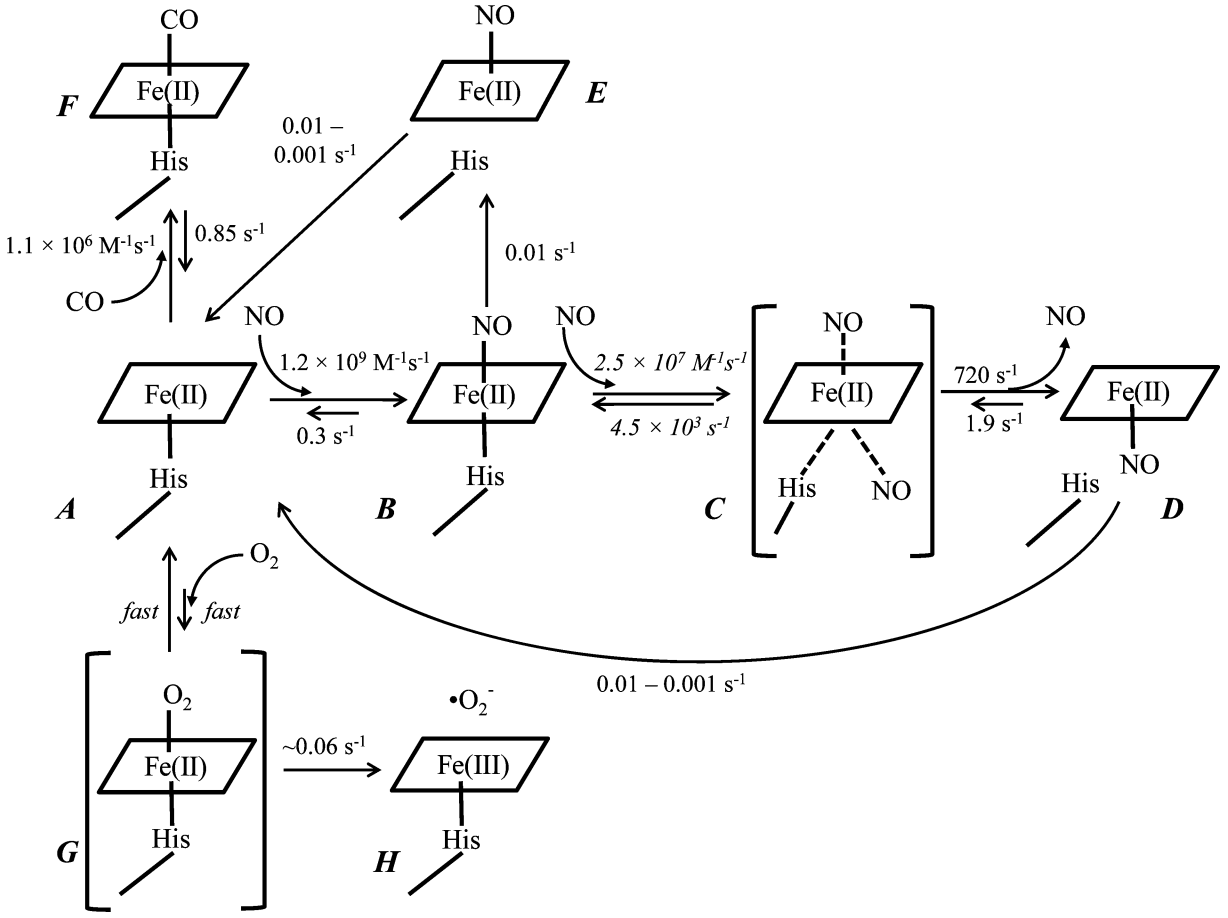

[a]Each heme species is labeled. The rate constants labeled in italic are estimated by simulation. Both association and dissociation of O_2 with Fe(II) *Vc* H-NOX are assumed to be fast, and the rate constants were not determined. Intermediates C and G (in brackets) are not observed in experiments and presumably exist only transiently. Intermediate C may be a quaternary complex as proposed in ref 8.

bandwidth of 5 nm, with a time constant of 0.5 s, at 0.5 nm resolution from 250 to 700 nm at a scan speed of 200 nm/min. Each spectrum is an average of 4−10 repetitive scans. Near-infrared MCD (NIR MCD) spectra between 700 and 1850 nm were obtained using a Jasco J-730W spectropolarimeter equipped with a 150 W tungsten halogen light, a high-sensitivity InSb detector cooled with liquid nitrogen, and a Jasco 1.4 T electromagnet. NIR MCD data were collected at room temperature at a bandwidth of 10 nm, with a time constant of 1 s, at 1 nm resolution and a scan speed of 500 nm/min. Each spectrum is an average of 12 or 16 scans. The MCD expressed in molar delta absorption coefficient, ΔA, in units of M^{-1} cm^{-1} T^{-1}, was calculated as $^1/_2[H^+(CD + MCD) - H^-(CD - MCD)]$ using the spectral analysis software that came with the instruments. MCD data between 500 and 700 nm were smoothed by the moving average algorithm performed using the same software.

The CO complex of *Vc* H-NOX was prepared by injecting the desired volume of CO-saturated anaerobic buffer (1 mM) into a cuvette containing Fe(II) *Vc* H-NOX sealed with an airtight septum. The NO complex was prepared similarly except that the NO stock (2 mM) was prepared in anaerobic water. The buffer used in all the experiments was 20 mM HEPES (pH 7.3) with 50 mM NaCl and 10% glycerol except in two situations. For the preparation of the NO complex, 50 mM TEA (pH 7.4) was used. In the NIR MCD experiment, samples of Fe(III) *Vc* H-NOX and its complexes were in 20 mM HEPES with 50 mM NaCl prepared in D_2O.

Stopped-Flow Experiments. The association and dissociation kinetics of gaseous ligands to anaerobic Fe(II) *Vc* H-NOX were studied by an Applied Photophysics (Leatherhead, U.K.) model SX-18MV stopped-flow instrument, and optically following the absorbance changes at different wavelengths with a monochromator or the whole spectral changes with a diode-array accessory. The sample handling unit was kept in an anaerobic chamber by COY Lab Products, Inc. (Grass Lake, MI). Ferrous *Vc* H-NOX used in all the experiments was prepared by sodium hydrosulfite titration after five cycles of vacuum and argon displacement in a tonometer. Diode-array data were analyzed with the global analysis method using the Pro-K package (Applied Photophysics). Observed rate constants, k_{obs}, of single-wavelength data under pseudo-first-order conditions ([L]/[*Vc* H-NOX] > 10) were obtained by fitting the profiles of optical changes to the standard exponential function:

$$A = A_f + a\, e^{-k_{obs}t} \quad (1)$$

where A_f is the final optical absorbance, t is the reaction time, and a is the amplitude of the change in reactions. Second-order association rate constant k_{on} and dissociation rate constant k_{off} were derived from the slope and y-intercept, respectively, in the secondary plots of k_{obs} versus gaseous ligand concentration [L]:

dx.doi.org/10.1021/bi401408x | *Biochemistry* 2013, 52, 9432−9446

$$k_{obs} = k_{on}[L] + k_{off} \quad (2)$$

In this study, k_{off} constants for the NO and CO complexes with *Vc* H-NOX are small and fitting errors prevent the extraction of their accurate values based on the *y*-intercepts of this type of plot. Dissociation constants were therefore determined using competition methods as explained in Results.

When the rate of formation of the 6c NO complex was measured, *Vc* H-NOX was mixed with an equal concentration of NO, and the k_{obs} was obtained by fitting the time-dependent optical change with the following equation:

$$A = A_f + A_0/(A_0 k_{obs} t + 1) \quad (3)$$

where A_0 is the initial optical absorbance. The second-order rate constant in units of M^{-1} s^{-1} was obtained by multiplying k_{obs} by the difference extinction coefficient.

EPR Spectroscopy. EPR spectra were recorded on a Bruker EMX spectrometer. Data analyses and spectral simulations were conducted using WinEPR and SimFonia furnished with the EMX system. Liquid nitrogen EPR (115 K) was conducted under the following conditions: frequency, 9.29 GHz; modulation frequency, 100 kHz; modulation amplitude, 2.0 G; and time constant, 0.33 s. The conditions for liquid helium EPR (10 K) were the same except for the frequency, 9.58 GHz, and the modulation amplitude, 5 or 10 G. The microwave power dependence was fit by nonlinear regression to the following equation:

$$\log(S/P^{1/2}) = (-b/2) \times \log(P_{1/2} + P) + (b/2) \times \log(P_{1/2}) + \log K \quad (4)$$

where P is the microwave power, S is the peak-to-trough amplitude of the EPR signal, $P_{1/2}$ is the microwave power at half-saturation, and b and K are floating parameters with b values of 1 and 3 for nonhomogeneous and homogeneous line broadening, respectively.[15] EPR samples of the Fe(II) *Vc* H-NOX−NO complex were prepared by rapidly mixing Fe(II) *Vc* H-NOX with desired levels of NO using a rapid freeze apparatus (Update Instrument, Madison, WI) placed inside an anaerobic chamber. The mixtures were shot into EPR tubes and freeze-trapped within 1−2 s in an ethanol/dry ice mixture.

Computer Modeling. Optical changes at 420 nm of the reaction of Fe(II) *Vc* H-NOX with NO under pseudo-first-order conditions were simulated using SCoP (Simulation Resources Inc., Redlands, CA). The model used was based in Scheme 1 (B ↔ C → D). Rate constants for the C → D reaction and extinction coefficients for both 6c and 5c *Vc* H-NOX−NO complexes were set to the values determined experimentally. The rate constants for the B ↔ C reaction and the extinction coefficient for the putative transient quaternary complex were allowed to float.

RESULTS

Expression and Purification of *Vc* H-NOX. The typical yield of purified *Vc* H-NOX from our bacterial expression was ~27 mg/L of cell culture, and the purity was estimated to be >95% based on SDS−PAGE (data not shown). The estimated molecular mass, 21.5 kDa, agrees well with the expected value.[12] Pyridine hemochrome analysis indicates a non-covalently bound *b*-type heme, with a stoichiometry of 0.94 ± 0.03 (n = 3) heme per *Vc* H-NOX monomer. The Soret absorption of purified *Vc* H-NOX is typically between 410 and 412 nm (data not shown). However, the Soret peak shifts to 406 nm upon oxidation by ferricyanide or to 428 nm upon reduction by sodium hydrosulfide, indicating the oxidation state of heme in purified *Vc* H-NOX is a mixture of ferric and ferrous states. The determined extinction coefficients of ferric and ferrous *Vc* H-NOX are 115.4 and 145 mM^{-1} cm^{-1}, respectively (Table S1 of the Supporting Information), similar to the published values.[12]

Electronic Absorption and MCD Spectroscopy of Fe(II) *Vc* H-NOX and Its Complexes with CO and NO. Ferrous *Vc* H-NOX exhibits a Soret band at 428 nm and a Q-band at 558 nm. Association of CO with Fe(II) *Vc* H-NOX shifts the Soret peak to 422 nm, with an extinction coefficient of 210.0 mM^{-1} cm^{-1}, and the Q-band splits into two maxima at 540 and 568 nm (Figure 1A and Table S1 of the Supporting Information). The wavelength of the Soret peak of the *Vc* H-NOX−CO complex is similar to those of myoglobin−CO (Mb−CO), sGC−CO, and *Ns* H-NOX−CO complexes, indicating a 6c low-spin heme (Scheme 1, F).[12,14,16] Mixing Fe(II) *Vc* H-NOX with an excess of NO shifts the Soret peak to 398 nm, with an extinction coefficient of 99.1 mM^{-1} cm^{-1}, and the Q-band to 572 nm with a shoulder at 538 nm (Figure 1A and Table S1 of the Supporting Information). The electronic absorption spectrum of the *Vc* H-NOX−NO complex is very similar to that of the 5c sGC−NO complex (Scheme 1, D).[8]

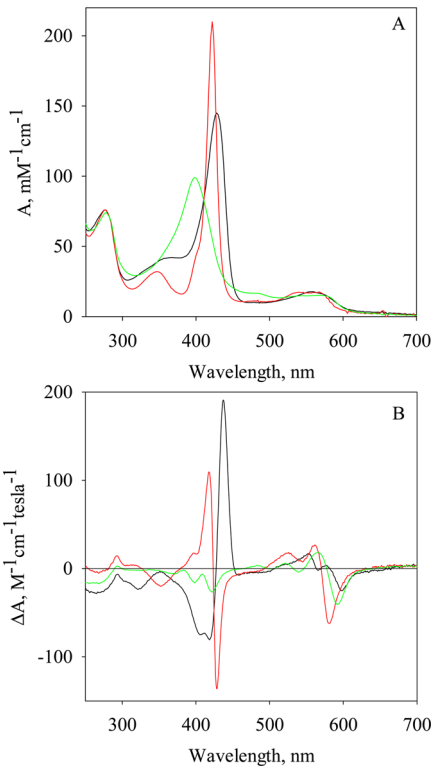

Figure 1. Electronic absorption and MCD spectra of Fe(II) *Vc* H-NOX and its complexes with CO and NO. The electronic absorption spectra (A) and MCD spectra (B) of Fe(II) *Vc* H-NOX (6.3 μM) and its complexes are represented using different colors: black for Fe(II) *Vc* H-NOX, red for the CO complex, and green for the 5c NO complex. The complexes were prepared using a [CO]/[*Vc* H-NOX] ratio of 6 and a [NO]/[*Vc* H-NOX] ratio of 4.

In the Soret region, the MCD spectrum of unliganded Fe(II) *Vc* H-NOX exhibits a split trough between 405 and 418 nm, with intensities of −70.7 to −76.1 M^{-1} cm^{-1} T^{-1}, and a peak at 437 nm, with an intensity of 180.4 M^{-1} cm^{-1} T^{-1} (Figure 1B

dx.doi.org/10.1021/bi401408x | *Biochemistry* 2013, 52, 9432−9446

and Table S1 of the Supporting Information). The crossover is at 427 nm, corresponding to the Soret peak of its electronic absorption spectrum. The line shapes of both Soret bands and Q-bands are similar to those of deoxymyoglobin,[17] indicating a high-spin ferrous heme in the unliganded Fe(II) *Vc* H-NOX. The MCD spectrum of the *Vc* H-NOX−CO complex exhibits a peak of 103.4 M^{-1} cm^{-1} T^{-1} at 428 nm and a tough of −128.3 M^{-1} cm^{-1} T^{-1} at 428 nm, with a crossover at 423 nm (Figure 1B and Table S1 of the Supporting Information). The line shapes of both Soret bands and Q-bands are very similar to those of the Mb−CO complex,[17] confirming a 6c low-spin heme in the *Vc* H-NOX−CO complex. The MCD of the *Vc* H-NOX−NO complex exhibits bands of significantly lower intensities compared to the intensities of the bands of Fe(II) *Vc* H-NOX and its CO complex, and the major signatures include a trough of −20.5 M^{-1} cm^{-1} T^{-1} at 399 nm and a derivative-shaped feature centered at 579 nm (Figure 1B and Table S1 of the Supporting Information). These features are similar to those observed for the H93G Mb−NO complex in the presence of 1 mM imidazole[17] and a 5c ferrous heme−NO model compound, verifying that the heme in the *Vc* H-NOX−NO complex in the presence of an excess of NO is in a 5c state (Scheme 1, D).

Kinetics of Binding of CO to Fe(II) *Vc* H-NOX. The binding of CO to Fe(II) *Vc* H-NOX is a simple reversible one-step reaction with no spectral intermediate upon examination by rapid-scanning stopped-flow spectrophotometry (data not shown). The kinetics of CO binding was determined by following the time courses at 423 nm under pseudo-first-order reaction conditions using ∼1.3 μM Fe(II) *Vc* H-NOX and varying CO concentrations from 50 to 500 μM at 24 °C (Figure 2A). The rate constants (k_{obs}) were obtained by fitting to a single-exponential function (eq 1). The plot of k_{obs} versus [CO] exhibits a linear dependence on [CO], and a second-order association rate constant [k_{on}(CO) = 1.1 × 10^6 M^{-1} s^{-1} (Table 1)] was obtained from the slope (eq 2 and Figure 2A, inset). The total absorbance changes are the same for all CO concentrations, indicating that complete saturation with CO was achieved with each [CO], and the K_D for CO binding is therefore ≪50 μM. The dissociation rate constant (k_{off}) was measured with the NO displacement method[18] by reacting the *Vc* H-NOX−CO complex with 1 mM NO and following the change in A_{423} (Figure 2B). Fitting the time course of A_{423} to eq 1 yielded a k_{off}(CO) of 0.85 s^{-1} (Figure 2B, inset, and Table 1). The equilibrium dissociation constant [K_D(CO)] is calculated to be 0.77 μM (Table 1).

Reaction of O_2 with Fe(II) *Vc* H-NOX. The Soret peak slowly shifted from 428 to 412 nm during the reaction of ∼3 μM Fe(II) *Vc* H-NOX with 600 μM O_2, followed by rapid-scanning stopped-flow spectrophotometry (Figure 3A). The ending wavelength is similar to that of resting *Vc* H-NOX (Figure 3A). In the same time period, the Q-band shifted from 558 to 534 nm (Figure 3A). No well-defined isosbestic point(s) was observed around the Soret peak, implying that multiple steps are involved in the transition. However, no intermediate with a clear sign of an Fe(II) heme−O_2 complex, which usually gives a split Q-band and a Soret peak at ∼415 nm,[16] is resolved from the spectral change. The spectral changes thus appear to be an autoxidation from Fe(II) *Vc* H-NOX to its ferric state, with very transient formation of the Fe(II) heme−O_2 complex (Scheme 1, G to H).

When 3 μM Fe(II) *Vc* H-NOX was reacted with O_2 at concentrations from 100 to 600 μM, the extents of change of

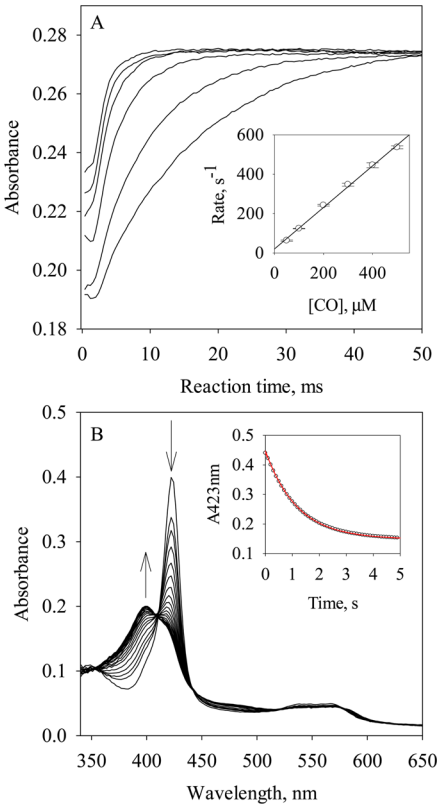

Figure 2. Determination of k_{on}(CO) and k_{off}(CO) for Fe(II) *Vc* H-NOX. (A) Time-dependent changes in A_{423} during the reactions of ∼1.3 μM Fe(II) *Vc* H-NOX with 50, 100, 200, 300, 400, and 500 μM CO (from bottom to top) at 24 °C. The inset shows the observed rate constants, k_{obs} (○), and the linear regression of the data. The error bars are the standard deviations of four individual measurements. (B) Time-dependent change in A_{423} during the reaction of ∼2.1 μM Fe(II) *Vc* H-NOX and 25 μM CO with 1 mM NO at 24 °C. The inset shows the time course of A_{423} (black). The red line represents the fit to eq 1.

Table 1. k_{on}, k_{off}, and K_D Values of Gaseous Ligands to Fe(II) *Vc* H-NOX

ligand	k_{on} (M^{-1} s^{-1})	k_{off} (s^{-1})	K_D (μM)
NO	1.1 × 10^9	0.3	2.7 × 10^{-4}
CO	1.1 × 10^6	0.85	0.77
O_2	–	–	(∼1.3 × 10^3)[a]

[a]Estimated on the basis of the K_D values of CO and NO and the sliding scale rule (Figure 12).

the time courses at 429 nm increased with O_2 concentration (Figure 3B), indicating no saturation was reached even at the highest O_2 concentration available with oxygenated buffer, and the K_D(O_2) to Fe(II) *Vc* H-NOX is therefore at least >600 μM. Each kinetic trace was fit well with one exponential function (eq 1), and the k_{obs} constants exhibit a linear dependence on O_2 concentration (Figure 3B, inset). The slope of k_{obs} versus O_2 concentration yielded a second-order reaction rate constant, 4.8 M^{-1} s^{-1}; on the basis of that value, the rate of autoxidation of Fe(II) *Vc* H-NOX to the ferric state was estimated to be ∼0.06 s^{-1} (see Discussion).

Binding of NO to Fe(II) *Vc* H-NOX. The rapid-scanning diode-array measurements of binding of NO to Fe(II) *Vc* H-NOX were conducted using either a stoichiometric amount (Figure 4A) or a 10-fold excess of NO versus Fe(II) *Vc* H-NOX (Figure 4B). A stoichiometric amount of NO binds to Fe(II) *Vc*

dx.doi.org/10.1021/bi401408x | *Biochemistry* 2013, 52, 9432−9446

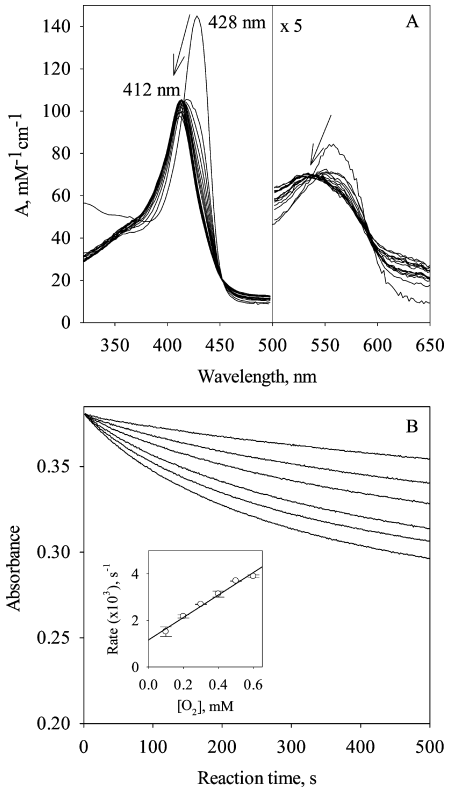

Figure 3. Autoxidation of Fe(II) *Vc* H-NOX by O_2. (A) Spectral changes during the reaction of 3 μM Fe(II) *Vc* H-NOX with 600 μM O_2 at 24 °C, monitored for 65.5 s. An absorption spectrum of Fe(II) *Vc* H-NOX, with a Soret peak at 428 nm, is presented as the starting point at 0 s. The absorption between 500 and 650 nm is scaled up by a factor of 5 for easy comparison (right). The slanted arrows indicate the directions of wavelength shift and the changes in amplitude. (B) Stopped flow of 3 μM Fe(II) *Vc* H-NOX with 0.1, 0.2, 0.3, 0.4, 0.5, and 0.6 mM O_2 at 24 °C (from top to bottom, respectively). The inset shows the observed rate constants, k_{obs} (○), plotted vs $[O_2]$ and fit via linear regression. The error bars are the standard deviations of four individual measurements.

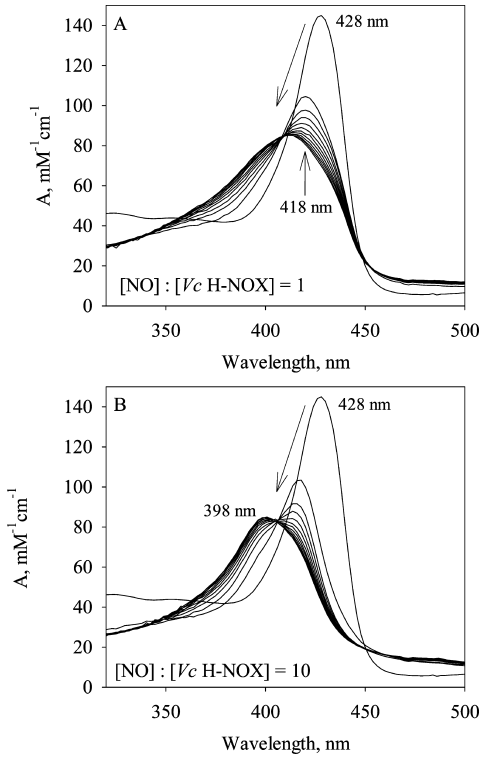

Figure 4. Spectral changes during binding of NO to Fe(II) *Vc* H-NOX. (A) Fe(II) *Vc* H-NOX (2.5 μM) was reacted with 2.5 μM NO at 24 °C, and the spectral change is shown up to 65.5 s. (B) Fe(II) *Vc* H-NOX (2.5 μM) was reacted with 25 μM NO at 24 °C, and the spectral change is shown up to 1 s. An absorption spectrum of Fe(II) *Vc* H-NOX, with a Soret peak at 428 nm, is presented in both panels as the starting spectrum at 0 s. The Soret peaks of the 6c *Vc* H-NOX–NO complex at 418 nm and the 5c *Vc* H-NOX–NO complex at 398 nm are labeled. The slanted arrows indicate the directions of wavelength shift and the changes in amplitude.

H-NOX in a single rapid phase, with the Soret peak shifting from 428 to 418 nm and an isosbestic point at 420 nm (Figure 5A). This indicates the formation of a 6c *Vc* H-NOX–NO complex (Scheme 1, B), similar to what was observed for *Ns* H-NOX and sGC.[5,8,14] Most of the reaction was lost in the 1.5 ms dead time of the stopped-flow apparatus, indicating a very large k_{on}(NO). The 418 nm Soret peak slowly shifted to 414 nm with an isosbestic point at 410 nm after ~1 min (Figure 4A) and continued to shift very slowly to 399 nm (data not shown). The overall conversion rate was ~0.01 s^{-1}, determined by global analysis. This suggests that the stoichiometric binding of NO to *Vc* H-NOX results in slow dissociation of the proximal histidine and a 5c NO–heme complex, with NO on the distal side of heme (Scheme 1, E). In the presence of an excess of NO, the formation of the 6c *Vc* H-NOX–NO complex was complete in the dead time of the stopped-flow apparatus and the Soret peak quickly shifted to 398 nm (Figure 4B), indicating conversion to a 5c *Vc* H-NOX–NO complex (Scheme 1, D). Although no intermediate(s) was resolved for *Vc* H-NOX, the formation of this 398 nm 5c *Vc* H-NOX–NO complex likely goes through a quaternary complex as proposed for the binding of NO to sGC (Scheme 1, C).[8]

To determine the large k_{on}(NO) of the 6c *Vc* H-NOX–NO complex, we measured the kinetics under true second-order reaction conditions, using a [NO]:[Fe(II) *Vc* H-NOX] ratio of 1:1 and a final concentration of 0.6 μM each, to avoid missing most of the time course in the dead time of the stopped-flow apparatus.[5] The measurements at 429 nm captured ~60% of the total expected changes. The observed time course was fit to a second-order, irreversible mechanism (eq 3, Figure 5A, inset) and yielded a k_{on}(NO) value of 1.1×10^9 M^{-1} s^{-1} (Table 1).

The dissociation rate constant, k_{off}(NO), of the initial 6c *Vc* H-NOX–NO complex, with a Soret peak at 418 nm, was measured using the sequential stopped-flow method.[5] The 6c *Vc* H-NOX–NO complex was generated by reacting 4.7 μM *Vc* H-NOX with 5 μM NO, and the formation of the 6c *Vc* H-NOX–NO complex was completed within 10 ms. The 6c NO complex was then aged for 50 ms and reacted with 0.5 mM CO in 12.5 mM dithionite to displace and consume the dissociated NO, respectively.[5] An exponential increase in A_{423} was observed following the second mixing (Figure 5B), indicating the formation of the 6c *Vc* H-NOX–CO complex. Fitting the time course at 423 nm to the single-exponential function (eq 1) yielded a rate constant k_{off}(NO) of 0.3 s^{-1} (Figure 5B, inset, and Table 1). This rate constant is much slower than k_{on}(CO) to Fe(II) *Vc* H-NOX (Figure 2, inset), indicating that the rate of NO displacement by CO is limited by the dissociation of NO from the 6c *Vc* H-NOX–NO complex. Combined with the

dx.doi.org/10.1021/bi401408x | *Biochemistry* 2013, 52, 9432–9446

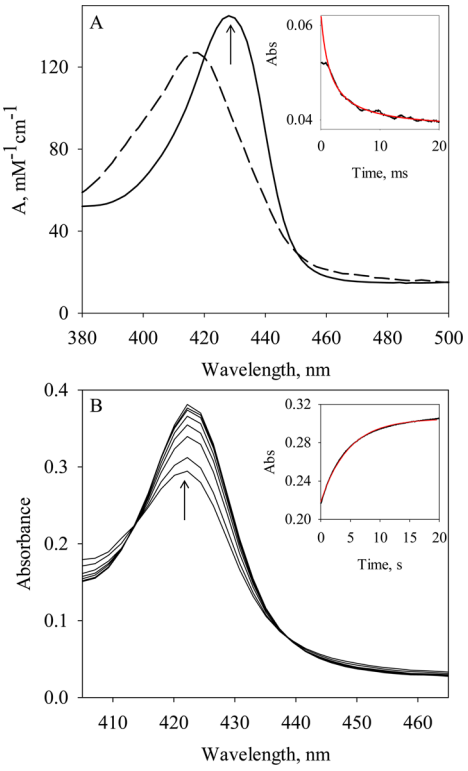

Figure 5. Determination of k_{on}(NO) and k_{off}(NO) in the formation of the 6c *Vc* H-NOX−NO complex. (A) The resolved absorption spectrum of the 6c *Vc* H-NOX−NO complex (−−−) in comparison with that of Fe(II) *Vc* H-NOX (—). Reaction of 0.6 μM Fe(II) *Vc* H-NOX with 0.6 μM NO at 24 °C. The arrow indicates the wavelength for measuring k_{on}(NO). The inset shows the time course of A_{429} (black). The red line represents the fit to a second-order reaction mechanism (eq 3). (B) Rapid-scanning stopped-flow of the dissociation of the 6c *Vc* H-NOX−NO complex. Fe(II) *Vc* H-NOX (9.4 μM) was first mixed with 10 μM NO, aged for 50 ms, and then further mixed with 1 mM CO in 25 mM dithionite. The inset shows the time course of A_{423} (black). The red line represents the fit to a single-exponential function (eq 1).

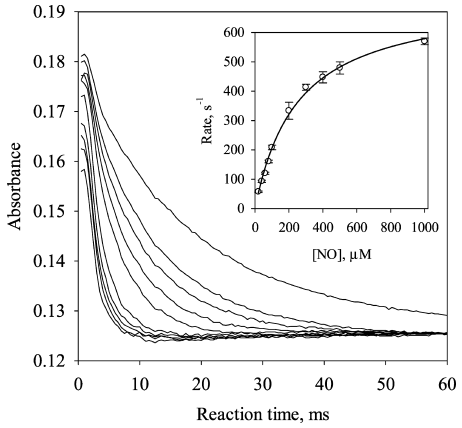

Figure 6. Saturation kinetics for the formation of the 5c *Vc* H-NOX−NO complex. Time courses of A_{420} during the reactions of ~1.8 μM Fe(II) *Vc* H-NOX with 20, 40, 60, 80, 100, 200, 300, 400, 500, and 1000 μM NO (from top to bottom, respectively) at 24 °C. The inset shows the observed rate constants, k_{obs} (○), plotted vs NO concentration and fit to eq 5.[51] The error bars are the standard deviations of four individual measurements.

k_{on}(NO) and k_{off}(NO) constants, the K_D(NO) for the 6c *Vc* H-NOX−NO complex is calculated to be 0.27 nM (Table 1).

With an excess of NO, the kinetics of the conversion from the 6c *Vc* H-NOX−NO complex to the 5c *Vc* H-NOX−NO complex, with a Soret peak at 398 nm, was measured by reacting Fe(II) *Vc* H-NOX with NO under pseudo-first-order conditions, and the time courses at 420 nm were followed (Figure 6). Under these experimental conditions, the formation of the 6c *Vc* H-NOX−NO complex was complete within the dead time of the stopped-flow apparatus and the k_{obs} values are the formation rate constants of the 5c *Vc* H-NOX−NO complex, which presumably forms through a quaternary complex (Scheme 1, B to D), as indicated by the EPR studies of binding of ^{14}NO and ^{15}NO to sGC.[8] When k_{obs} values are plotted versus NO concentration, a linear dependence on NO concentration is observed at NO concentrations of <50 μM (data not shown), and at higher NO concentrations, the dependence gradually levels off (Figure 6, inset). This is very different from what was observed for sGC, where k_{obs} for the formation of the 5c sGC−NO complex always exhibited a linear dependence on NO concentration, indicating a transition from the hypothetical quaternary complex (corresponding to C in Scheme1) to the 5c sGC−NO complex is never rate-limiting.[8] For Fe(II) *Vc* H-NOX, the hyperbolic saturation phenomenon of k_{obs} versus NO concentration strongly suggests that the 5c *Vc* H-NOX−NO complex forms through a transient quaternary complex, as represented in reactions I and II:

$$\text{6c NO-heme-His} + \text{NO} \Leftrightarrow \text{NO-heme−NO(−His)} \quad (k_1, k_{-1}) \qquad \text{(I)}$$

$$\text{NO-heme−NO(−His)} \Leftrightarrow \text{5c heme-NO} \quad (k_2, k_{-2}) \qquad \text{(II)}$$

At very high [NO], reaction II becomes rate-limiting, and k_2 = 720 s^{-1} is determined by fitting the k_{obs} versus [NO] plot with the following hyperbolic function (Figure 6, inset):

$$k_{obs} = k_2 \times [NO]/(K_M + [NO]) + k_{-2} \qquad (5)$$

The estimated K_M was 250 μM by fitting. Here the rate constant for reassociation of NO with 5c *Vc* H-NOX to form the NO−heme−NO(−His) complex (k_{-2} = 1.9 s^{-1}) was obtained from the *y*-intercept of the plot of k_{obs} versus low NO concentration (data not shown). A computer model was built on the basis of reactions I and II to simulate the kinetic events during the formation of the 5c *Vc* H-NOX−NO complex. Satisfactory simulation was obtained with k_1 and k_{-1} set to 2.5 × 10^7 M^{-1} s^{-1} and 4.5 × 10^3 s^{-1}, respectively (Figure S1 of the Supporting Information).

The dissociation rate constants, k_{off}, of the 5c *Vc* H-NOX−NO complexes in the presence of both stoichiometric NO or an excess of NO were measured by the displacement of NO with CO.[19] In the presence of an excess of NO, 6.7 μM Fe(II) *Vc* H-NOX was first reacted with 30 μM NO, and the generated 5c *Vc* H-NOX−NO complex was next reacted with 0.5 mM CO in 12.5 mM dithionite. The Soret peak shifted from 398 nm to that of the 6c *Vc* H-NOX−CO complex (Figure 7). The time course at 422 nm indicates that the NO displacement is a biphasic process, and fitting to a double-exponential function yielded rate constants of 0.01 s^{-1} (29% overall reaction) and 0.001 s^{-1} (71% overall reaction) (Figure 7, inset). In the presence of a stoichiometric amount of NO, the displacement of NO from the 5c *Vc* H-NOX−NO complex is also a biphasic process with the same rates, 0.01 s^{-1} (16% overall reaction) and 0.001 s^{-1} (84% overall reaction) (data not shown). In both cases, the kinetics of NO displacement was the

dx.doi.org/10.1021/bi401408x | *Biochemistry* 2013, 52, 9432−9446

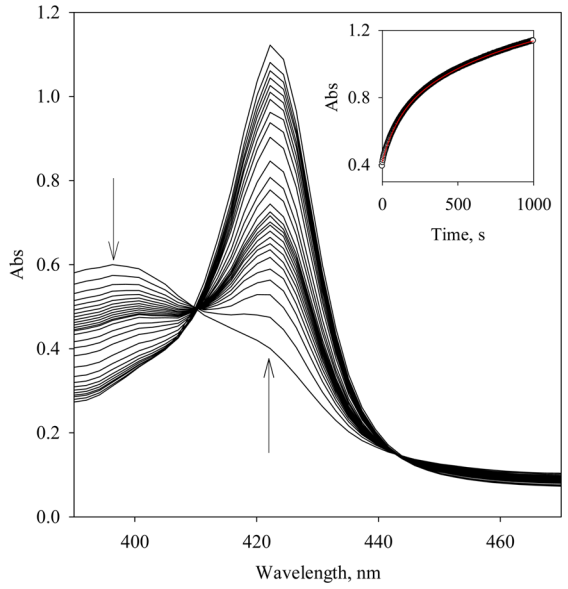

Figure 7. Determination of the dissociation of the 5c *Vc* H-NOX−NO complex. The spectral change during the rapid-scanning stopped-flow reaction, 13.4 μM Fe(II) *Vc* H-NOX and 60 μM NO mixed with 1 mM CO and 25 mM dithionite, is presented. The arrows indicate the directions of absorbance changes. The inset shows the time courses of A_{422} (○) and a fit to double-exponential function $A = A_f + a_1e^{-(k_{obs,1})t} + a_2e^{-(k_{obs,2})t}$ (red line).

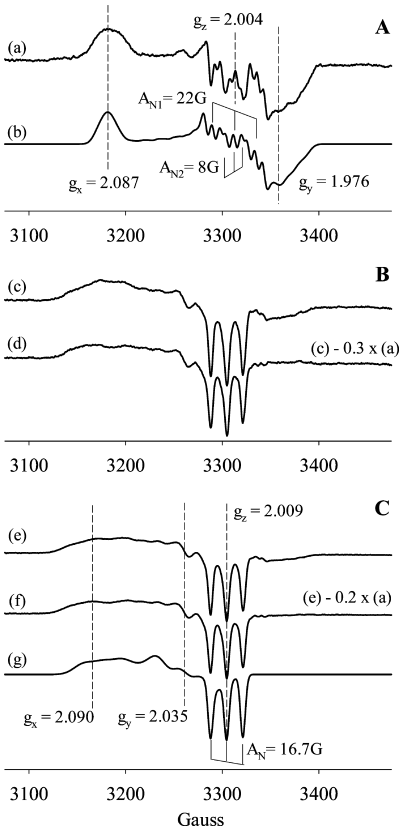

Figure 8. EPR spectra of Fe(II) *Vc* H-NOX−NO complexes. (A) (a) EPR of the 6c *Vc* H-NOX−NO complex, prepared by freeze-trapping of 39 μM Fe(II) *Vc* H-NOX with NO in a 1:1 ratio for 1 s. (b) Simulation of the 6c NO−heme complex using the following parameters: g_x = 2.087, g_y = 1.976, g_z = 2.004; A_x = 6 G, A_y = 12 G, and A_z = 22.2 G (for A_{N1}); A_x = 6 G, A_y = 12 G, and A_z = 8 G (for A_{N2}). (B) (c) EPR of the 5c *Vc* H-NOX−NO complex, prepared by freeze-trapping of 39 μM Fe(II) *Vc* H-NOX with NO in a 1:1 ratio for 30 s. (d) EPR spectrum of an approximately pure 5c heme−NO complex, obtained by subtracting ∼30% of spectrum a from spectrum c. (C) (e) EPR of the *Vc* H-NOX−NO complex, prepared by freeze-trapping of 39 μM Fe(II) *Vc* H-NOX with NO in a 1:10 ratio for 10 s. (f) EPR of an approximately pure 5c *Vc* H-NOX−NO complex obtained by subtracting 20% of spectrum a from spectrum e. (g) Simulation of the 5c NO−heme complex using the following parameters: g_x = 2.090, g_y = 2.035, g_z = 2.009; A_x = 20 G, A_y = 22 G, and A_z = 16.7 G (for A_N).

same with 50 mM dithionite (data not shown), indicating that the rates of formation of the *Vc* H-NOX−CO complex in these measurements are limited by the dissociation of the 5c *Vc* H-NOX−NO complexes. The biphasic dissociation of the 5c *Vc* H-NOX−NO complexes is probably caused by the existence of two different conformations.

EPR Characterization of the Fe(II) *Vc* H-NOX−NO Complex. EPR exhibited features of a typical 6c NO complex when Fe(II) *Vc* H-NOX was reacted with NO in a 1:1 ratio and freeze-trapped after 1 s (Figure 8A, spectrum a). This is consistent with the rapid-scanning stopped-flow observation (Figure 4A). The nine-line hyperfine splitting of the g_z component can be fit using two different nuclear spin = 1 hyperfine splittings of 22.2 and 8 G for the nitrogen atoms of NO and the proximal histidine ligand, respectively (Figure 8A, spectrum b). EPR of the sample freeze-trapped after reaction for 30 s revealed mainly a 5c high-spin NO complex with minor features due to a 6c NO complex (Figure 8B, spectrum c). Subtraction of ∼30% 6c heme−NO EPR yields the spectrum of an almost pure 5c heme−NO complex (Figure 8B, spectrum d), presumably with NO ligated to the distal side of the heme (Scheme 1, E). The conversion rate observed in the rapid-freeze EPR experiment was significantly faster than that measured with rapid-scanning stopped-flow spectrophotometry (Figure 4A). This could be due to the much higher Fe(II) *Vc* H-NOX and NO concentrations and much lower temperatures used in the rapid-freeze EPR compared to those used in stopped-flow spectrophotometry. These different experimental conditions may significantly affect the equilibrium between the 6c and 5c *Vc* H-NOX−NO complexes.

The EPR spectrum of the freeze-trapped sample from the reaction of Fe(II) *Vc* H-NOX with NO in a 1:10 ratio is dominated by a 5c high-spin signal with three distinct hyperfine features contributed by the nitrogen nucleus of NO (Figure 8C, spectrum e). This is consistent with the optical data (Figures 1A and 4B). The signal of a small portion of the 6c heme−NO complex can still be observed, and subtraction of ∼20% of the 6c heme−NO EPR yields the spectrum of an almost pure 5c heme−NO complex (Figure 8C, spectrum f). The spectrum of such a 5c complex can be fit using a g_z hyperfine splitting constant of 16.7 G (Figure 8C, spectrum g). The EPR features of 5c NO complexes generated with 1 × NO and 10 × NO appear to be very similar (Figure 8, spectra d and f), different from the case of sGC in which two different sets of 5c NO−heme EPR signatures are detected.[20,21] A microwave power dependence study on the 5c *Vc* H-NOX−NO complex yielded a half-saturation power of 138 mW and a line broadening factor of 1.6 (data not shown), close to that of inhomogeneous line broadening.[22] The large half-saturation power indicates the presence of a fast energy relaxation mechanism via strong spin−orbital coupling.

dx.doi.org/10.1021/bi401408x | *Biochemistry* 2013, 52, 9432−9446

Electronic Absorption and MCD Spectroscopy of Fe(III) *Vc* H-NOX and Its Complexes. H-NOX family proteins are likely sensors for gaseous ligands based on the measured selective binding of gaseous ligands and structural homology to sGC. However, the presence of both stable ferric and ferrous states of the purified recombinant *Vc* H-NOX and the major conformational adjustment during the transition from the ferrous to the ferric state observed for *Ns* H-NOX suggests another possible role of redox sensing of these proteins.[14] We therefore also characterized *Vc* H-NOX in its ferric state and its complexes with different ligands.

Ferric *Vc* H-NOX exhibits a Soret peak at 406 nm of 115.4 mM^{-1} cm^{-1}, a Q-band at 522 nm, and a ligand-to-iron or porphyrin-to-iron charge-transfer band at 636 nm, which is characteristic of high-spin heme species (Figure 9A). The binding of imidazole or cyanide shifts the Soret peak to longer wavelengths with increased intensities, 414 nm (149.3 mM^{-1} cm^{-1}) and 420 nm (125.7 mM^{-1} cm^{-1}), respectively (Figure 9A and Table S1 of the Supporting Information). The Q-bands of *Vc* H-NOX−Im and *Vc* H-NOX−CN^- complexes also shift to longer wavelengths, 534 and 538 nm, respectively, with similar intensities (Table S1 of the Supporting Information). The charge-transfer band cannot be observed for either complex. The wavelength and high intensities of the Soret bands and the absence of a charge-transfer band indicate that the coordination of imidazole or cyanide to Fe(III) *Vc* H-NOX converts heme to a fully low-spin state. Compared to that of imidazole and cyanide, the binding of fluoride and azide to Fe(III) *Vc* H-NOX is much weaker. In the presence of >200 mM fluoride or azide, the Soret peak shifts to shorter wavelengths, 400 nm (117.3 mM^{-1} cm^{-1}) and 394 nm (109.3 mM^{-1} cm^{-1}), respectively (Figure 9A and Table S1 of the Supporting Information). The Soret peak of the *Vc* H-NOX−N_3^- complex is quite broad. Compared to that of Fe(III) *Vc* H-NOX, the Q-bands of *Vc* H-NOX−F^- and *Vc* H-NOX−N_3^- complexes shift to longer wavelengths, 516 and 504 nm, respectively (Figure 9A). Similar to unliganded Fe(III) *Vc* H-NOX, these two complexes show charge-transfer bands at 604 and 628 nm, respectively (Figure 9A and Table S1 of the Supporting Information). The wavelengths of Soret peaks and the presence of charge-transfer bands clearly indicate high-spin hemes in *Vc* H-NOX−F^- and *Vc* H-NOX−N_3^- complexes. The spin state of the *Vc* H-NOX−N_3^- complex is different from the low-spin state observed in the Mb−N_3^- complex.[23]

As its electronic absorption spectrum, the MCD spectrum of Fe(III) *Vc* H-NOX also indicates predominantly high-spin heme as revealed by the presence of a charge-transfer band between 650 and 690 nm (Figure 9B and Table S1 of the Supporting Information). Compared to that of unliganded Fe(III) *Vc* H-NOX, the MCD spectra of *Vc* H-NOX−Im and *Vc* H-NOX−CN^- complexes exhibit significantly stronger Soret bands (Figure 9B), and Q-bands are observed at longer wavelengths with stronger intensities, at 582 nm (−19.5 M^{-1} cm^{-1} T^{-1}) and 578 nm (−26.6 M^{-1} cm^{-1} T^{-1}) for *Vc* H-NOX−Im and *Vc* H-NOX−CN^- complexes, respectively (Figure 9B and Table S1 of the Supporting Information). The *Vc* H-NOX−Im complex also exhibits a peak of 8.1 M^{-1} cm^{-1} T^{-1} at 556 nm (Figure 9B). The relative intensities of the Soret bands and Q-bands between the Im and CN^- complexes of *Vc* H-NOX are similar to that between the Im and CN^- complexes of metMb.[24,25] No charge-transfer band in the range of 600−700 nm is observed, confirming the low-spin state of heme in these two complexes (Figure 9B).

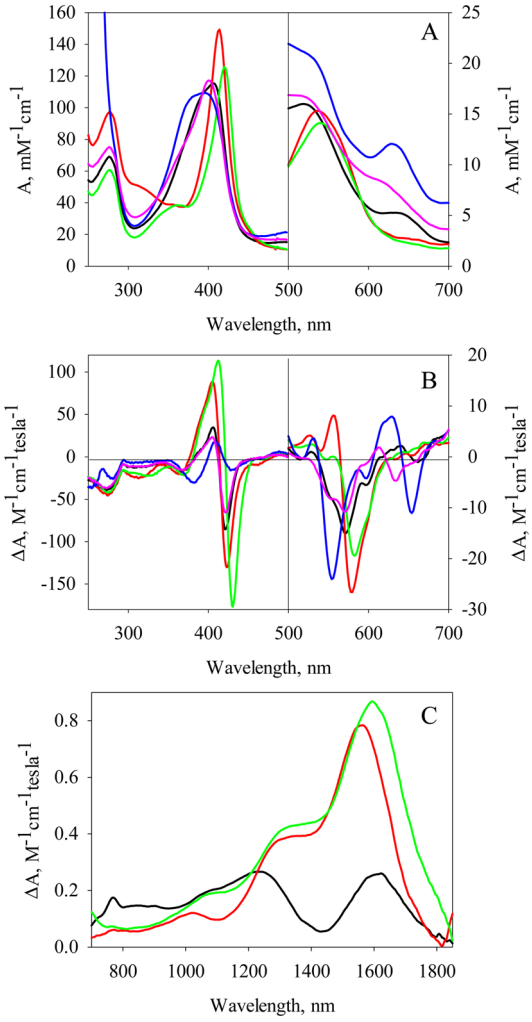

Figure 9. Electronic absorption and MCD spectra of Fe(III) *Vc* H-NOX and its complexes with CN^-, Im, F^-, and N_3^-. Electronic spectra (A) and MCD spectra (B) of ∼5 μM Fe(III) *Vc* H-NOX alone and in the presence of 1.4 mM CN^-, 200 mM Im, 500 mM F^-, and 200 mM N_3^-. The MCD spectra in the range of 500−700 nm was smoothed using the program that came with the instrument. (C) NIR MCD spectra of ∼85 μM Fe(III) *Vc* H-NOX alone and in the presence of 200 mM Im or 5.5 mM CN^-. The samples for NIR MCD were in 20 mM HEPES with 50 mM NaCl buffer prepared in D_2O. Spectra in panels A−C are represented with the same set of colors: black, Fe(III) *Vc* H-NOX; red, *Vc* H-NOX−Im complex; blue, *Vc* H-NOX−N_3^- complex; green, *Vc* H-NOX−CN^- complex; magenta, *Vc* H-NOX−F^- complex.

The MCD spectrum of the *Vc* H-NOX−F^- complex exhibits Soret bands and Q-bands at wavelengths similar to those of unliganded *Vc* H-NOX but with lower intensities, and a charge-transfer band is present in the range of 610−660 nm (Figure 9B and Table S1 of the Supporting Information), consistent with a high-spin heme as indicated by its electronic absorption spectrum. The Soret MCD signal of the *Vc* H-NOX−N_3^- complex is significantly smaller than those of *Vc* H-NOX and its other complexes (Figure 9B). This is different from the case for the metMb−N_3^- complex, whose MCD exhibits a Soret band slightly smaller than those of its Im and CN^- complexes.[24,25] The MCD of the *Vc* H-NOX−N_3^- complex exhibits a strong Q-band at the shortest wavelength among Fe(III) *Vc* H-NOX and its complexes, −24.0 M^{-1} cm^{-1} T^{-1} at 554 nm and the strongest charge-transfer band between 630 and 680 nm

dx.doi.org/10.1021/bi401408x | *Biochemistry* 2013, 52, 9432−9446

(Figure 9B and Table S1 of the Supporting Information). These MCD features are in sharp contrast to those of the metMb−N_3^- complex that exhibits a Q-band comparable to that of the metMb−Im complex and a very weak charge-transfer band at 647 nm[24] but overall similar to those in the prostaglandin H synthase−N_3^- complex that possesses a considerable amount of high-spin heme.[26] The MCD of the *Vc* H-NOX−N_3^- complex is therefore consistent with a high-spin heme.

The NIR MCD of Fe(III) *Vc* H-NOX exhibits two ligand-to-metal charge-transfer (LMCT) bands, one at 1619 nm and the other at 1232 nm (Figure 9C). Compared to those of *Ns* H-NOX,[14] the MCD signals of *Vc* H-NOX are of significantly lower intensities (Table S1 of the Supporting Information). Although the electronic absorption spectrum, visible region MCD, and EPR (see below) all indicate that the Fe(III) *Vc* H-NOX heme is largely high-spin, its NIR MCD is significantly different from that typical for a high-spin ferric heme such as that in metMb (metMb−H_2O), which exhibits a weak derivative shape MCD signal around 1150 nm.[27,28] When binding occurs with CN^- and Im, the intensities of the two NIR MCD bands increase significantly (Figure 9C and Table S1 of the Supporting Information), resulting in NIR MCD spectra similar to that of *Ns* H-NOX.[14] In the presence of Im, the NIR MCD of the Fe(III) *Vc* H-NOX−Im complex exhibits a LMCT band at 1563 nm with a shoulder at 1355 nm (Figure 9C). These features are typical for a bis-histidine low-spin ferric heme complex.[27,29−31] The overall similarity between the MCD of Fe(III) *Vc* H-NOX and its Im complex suggests that Fe(III) *Vc* H-NOX may contain ∼25% low-spin heme because of the distal histidine coordination. Compared to that of the Fe(III) *Vc* H-NOX−Im complex, the LMCT band of the Fe(III) *Vc* H-NOX−CN^- complex is centered at a longer wavelength at 1594 nm with a shoulder at 1372 nm (Figure 9C), consistent with the NIR CT band for the CN^-/histidine-ligated heme occurring at a wavelength of ∼1600 nm.[27]

EPR Characterization of Fe(III) *Vc* H-NOX and Its Complexes. EPR signatures for both high-spin and low-spin ferric hemes are observed for the resting *Vc* H-NOX (Figure 10), consistent with the electronic absorption and MCD data (data not shown). The high-spin signal is heterogeneous, containing both a rhombic component (g_x = 6.23, and g_y = 5.49) and an axial component ($g_x = g_y$ = 5.93). The g_z for both high-spin heme geometries is observed at 1.99 (Figure 10). For low-spin Fe(III) *Vc* H-NOX, g_{max} = 2.92 and g_{mid} = 2.26 signals are more visible (Figure 10), and the third *g* component predicted to be at 1.50 (g_{min}) is not visible for its broad line width. These low-spin signals are unlikely due to the ligation to heme by the Im used in the *Vc* H-NOX purification because the Im concentration in the resting *Vc* H-NOX after the removal of Im by desalting chromatography was much lower than its K_D for Fe(III) *Vc* H-NOX, 4.2 mM, measured by titration (data not shown). The correlation between its heme rhombicity and the ligand tetragonal field strength of the low-spin Fe(III) *Vc* H-NOX based on its *g* values puts it in zone B of the "truth diagram" (Figure 11).[15,32] This indicates that the axial ligand in low-spin Fe(III) *Vc* H-NOX is likely a histidine,[15,32] as proposed for low-spin Fe(III) *Ns* H-NOX[14] and suggested by the MCD of Fe(III) *Vc* H-NOX (Figure 9C). However, His150, which is proposed to be the axial ligand in low-spin Fe(III) *Ns* H-NOX, is not conserved in *Vc* H-NOX. On the other hand, the truth diagram of the Fe(III) *Vc* H-NOX−Im complex can be superimposed with that of as-isolated low-spin

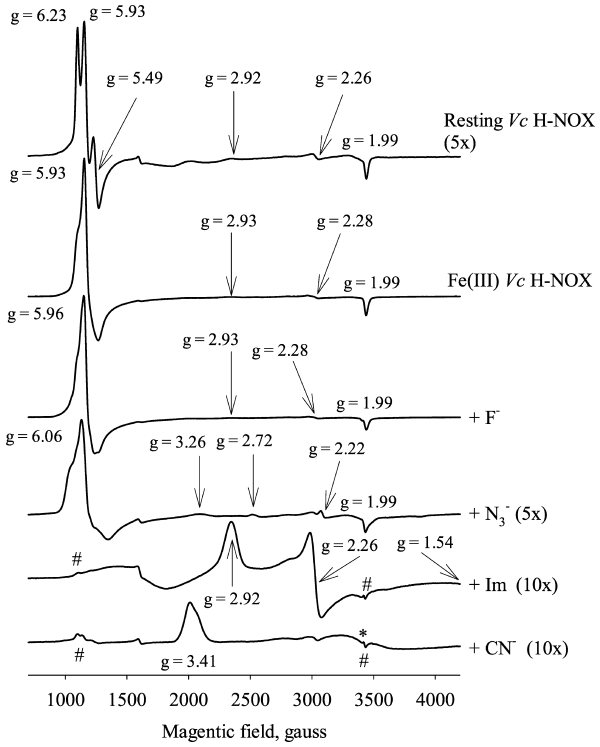

Figure 10. EPR spectra of Fe(III) *Vc* H-NOX and its complexes. The spectra were recorded at 10 K. "Resting *Vc* H-NOX" is the purified *Vc* H-NOX without further treatment. "Fe(III) *Vc* H-NOX" is the ferricyanide-oxidized *Vc* H-NOX. The various complexes were prepared using Fe(III) *Vc* H-NOX, by adding ligands to the following final concentrations: cyanide, 21 μM; imidazole, 196 mM; azide, 512 mM; and fluoride, 794 mM. Some spectra are magnified with the factors specified in parentheses for easy comparison. The important *g* values of each spectrum are marked. The # sign indicates the residual high-spin signals in Im and CN^- complexes, and the * sign indicates the possible g_{mid} of the low-spin heme in the CN^- complex.

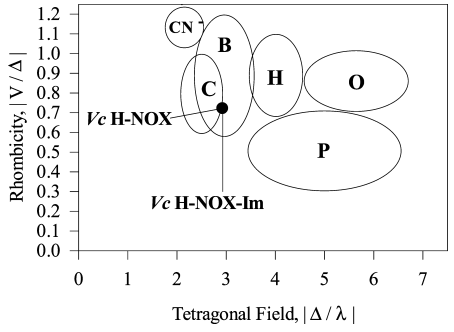

Figure 11. Truth diagram analysis of low-spin Fe(III) *Vc* H-NOX. Six zones, in mapping the correlation between the heme rhombicity and the axial ligand field strength of low-spin heme complexes, are labeled with various letters. Five zones contain the complexes with histidine as the proximal ligand but different distal ligands: cyanide (zone CN^-), methionine (zone C), histidine (zone B), imidazolate/azide (zone H), and hydroxide/phenolate (zone O). Zone P contains proteins that have a cysteine thiolate proximal ligand. The position of low-spin Fe(III) *Vc* H-NOX is represented by a solid circle and is superimposed with that of the Fe(III) *Vc* H-NOX−Im complex.

Fe(III) *Vc* H-NOX (Figure 11), suggesting that the axial ligand in resting low-spin Fe(III) *Vc* H-NOX is possibly still a histidine residue. In a structure of Fe(III) *Vc* H-NOX modeled against the crystal structure of Fe(II) *Ns* H-NOX, the closest

dx.doi.org/10.1021/bi401408x | *Biochemistry* 2013, 52, 9432−9446

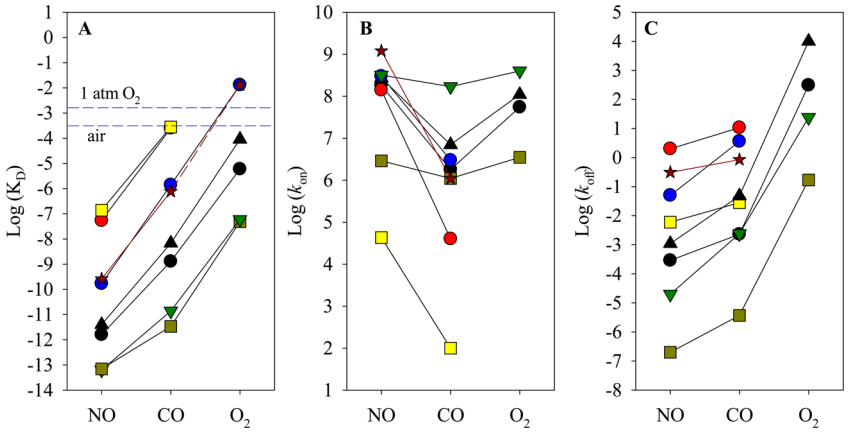

Figure 12. Relationship of log K_D, log k_{on}, and log k_{off} of NO and CO for Fe(II) *Vc* H-NOX vs ligand type. The measured logarithm values of K_D (A), k_{on} (B), and k_{off} (C) of NO and CO with respect to Fe(II) *Vc* H-NOX are plotted vs ligand type (dark red stars and solid dark red line). (A) The predicted log $K_D(O_2)$ is connected to log K_D(CO) by a dark red dashed line. Parameters measured for some other heme sensors and heme model Fe(II) PP(1-MeIm) are plotted for comparison and to show the large dynamic range of K_D, k_{on}, and k_{off} values modulated by the different heme binding environments: cytochrome *c′* (yellow square), *Ns* H-NOX (blue circle), sGC (red circle), H64V Mb (black triangle), L16A cytochrome *c′* (light green square), H61L leghemoglobin (Lb) (green triangle), and Fe(II) PP(1-MeIm) (black circle). The values for these heme sensors can be found in ref 5 and the references cited therein.

histidine on the distal side of heme is His77, which is ∼11 Å from iron. If His77 does coordinate with heme in low-spin Fe(III) *Vc* H-NOX, reduction may cause some significant movement of His77. Similar connection of such drastic conformational rearrangements to the subsequent signal transduction is proposed for *Ns* H-NOX during its redox state change.[14]

After the resting *Vc* H-NOX had been oxidized with ferricyanide, the rhombic component of the high-spin heme in Fe(III) *Vc* H-NOX decreases noticeably, now observed as a shoulder of the EPR signal of the axial heme at g = 5.93 (Figure 10). Concomitantly, the size of the axial EPR signal increases significantly. Two EPR features (g_{max} = 2.93, and g_{mid} = 2.28) are also visible for the low-spin heme for the ferricyanide-treated *Vc* H-NOX (Figure 10).

The formation of the Fe(III) *Vc* H-NOX−Im complex abolishes most of the high-spin heme signals, leading to a predominant low-spin heme with three principal g values at 2.92, 2.26, and 1.54 (Figure 10), indicating the formation of a 6c bis-imidazole heme complex. The truth diagram of the Fe(III) *Vc* H-NOX−Im complex overlaps exactly with that of resting low-spin Fe(III) *Vc* H-NOX (Figure 11), indicating that the axial ligand field and the rhombicity of the heme in the Fe(III) *Vc* H-NOX-Im complex are very similar to those in resting low-spin *Vc* H-NOX.[15,32] Like the EPR features of the Im complex, the Fe(III) *Vc* H-NOX−CN^- complex exhibits EPR of predominant low-spin heme. On the other hand, only an abnormally large g_{max} value of 3.41 was observed, similar to that of the metMb−CN^- complex,[33] indicating that the low-spin heme in the *Vc* H-NOX−CN^- complex is of a highly axial geometry.[34] This type of heme has been observed in the CN^- complexes of many other hemoproteins.[35−41] The values of the other two g components, g_{mid} and g_{min}, are not determined because of the overlap with the residual high-spin g_z value (Figure 10) and the fact that it is out of range of the data collection, respectively. The EPR signal of the Fe(III) *Vc* H-NOX−CN^- complex is of smaller amplitude compared to those of the Im complex. This is likely due to the increased anisotropy in the **g** tensor.[42]

The binding of F^- to Fe(III) *Vc* H-NOX does not fully convert the portion of the low-spin heme in Fe(III) *Vc* H-NOX to high-spin, even at F^- concentrations as high as 790 mM. This is indicated by the only partially split g = 1.99 signal, which is due to the $I = {}^1/_2$ nucleus spin of ^{19}F, and the visible low-spin g_{max} = 2.93 and g_{mid} = 2.28 signals (Figure 10). Some rhombic high-spin heme geometry can still be observed in the presence of a high concentration of F^-, as indicated by the shoulder of the g = 5.96 signal (Figure 10). In the presence of 512 mM N_3^-, the intensity of EPR of the high-spin heme decreases significantly but still dominates the EPR spectrum, indicating N_3^- does not convert Fe(III) *Vc* H-NOX to the low-spin state effectively, consistent with the electronic absorption and MCD data (Figure 9A,B). This is different from the fact that N_3^- completely converts metMb to the low-spin state.[23] The axial high-spin signal shifts slightly toward a lower frequency to a g = 6.06 signal (Figure 10). The EPR signal of rhombic high-spin heme increases as suggested by the more noticeable shoulders around the axial high-spin signal (Figure 10). Two sets of weak EPR signatures for low-spin heme were observed for the Fe(III) *Vc* H-NOX−N_3^- complex. One set has g values similar to those of the metMb−N_3^- complex: g_{max} = 2.72, and g_{mid} = 2.22;[23,33] the other set has a g_{max} = 3.26 signal for a heme geometry with a much lower rhombicity.

DISCUSSION

The mechanisms of binding of a gaseous ligand to Fe(II) *Vc* H-NOX could be summarized in Scheme 1 based on our spectroscopic and kinetic data (Table 1). CO binds *Vc* H-NOX in a reversible one-step process (A to F). NO, on the other hand, binds *Vc* H-NOX in multiple steps. A stoichiometric amount of NO binds to *Vc* H-NOX quickly and forms a 6c NO−*Vc* H-NOX−His complex (A to B), and the subsequent breakage of the proximal histidine coordination to iron leads to a 5c *Vc* H-NOX−NO complex (B to E). In the presence of an excess of NO, a second NO molecule binds to *Vc* H-NOX, presumably forming a transient quaternary complex (B to C), which is quickly converted to a 5c *Vc* H-NOX−NO complex with likely the distal NO ligands released (C to D) similar to that found in sGC using $^{15}NO/^{14}NO$ and freeze quench EPR.[8]

dx.doi.org/10.1021/bi401408x | *Biochemistry* 2013, 52, 9432−9446

When Fe(II) *Vc* H-NOX is reacted with O_2, the equilibrium is biased toward the reactants (A); however, autoxidation leading to Fe(III) *Vc* H-NOX appears to proceed slowly (G to H), without accumulation of the transient oxyferrous complex.

When affinities of NO and CO for Fe(II) *Vc* H-NOX (Table 1) are plotted versus ligand type, the line connecting the values of log K_D(NO) and log K_D(CO) can almost be superimposed with that of *Ns* H-NOX and parallels those of sGC and many heme sensor proteins and heme model Fe(II) PP(1-MeIm)[5] (Figure 12A). This clearly indicates that the selectivity of Fe(II) *Vc* H-NOX for gaseous ligands follows the same pattern seen for sGC and *Ns* H-NOX and is also consistent with the sliding scale rule hypothesis. On the basis of the sliding scale rule, the affinity of O_2 for Fe(II) *Vc* H-NOX can be predicted to be similar to that for *Ns* H-NOX, ~13 mM (Figure 12A, dashed line, and Table 1). In the plots of kinetic parameters versus ligand type, the line connecting log k_{on}(NO) and log k_{on}(CO) and the line connecting log k_{off}(NO) and log k_{off}(CO) approximately parallel those of sGC, *Ns* H-NOX, and many other heme sensor proteins and heme model Fe(II) PP(1-MeIm)[5] (Figure 12B,C).

With high affinities and multiple steps in NO binding and exclusion of O_2 binding, the characteristics of gaseous ligand binding are overall quite similar among *Vc* H-NOX, sGC, and *Ns* H-NOX. However, a few obvious differences exist in the binding of NO and O_2 to these three heme sensor proteins. One such difference is noticed in the binding of the second NO to these three proteins. In sGC, in the presence of NO at a 1:1 ratio, the 6c NO−heme−His complex is quickly converted to the 5c heme−NO complex with a Soret peak at 399 nm, which later oscillates between the 5c heme−NO complex and Fe(II) sGC.[43] Such an oscillation phenomenon was not observed for *Ns* H-NOX in the presence of a stoichiometric amount of NO, and its 6c NO−heme−His complex appears to be stable.[14] Similar to sGC, the 6c NO−heme−His complex in *Vc* H-NOX is not stable, as indicated by the shift of the Soret peak from 418 to 399 nm, which is mostly a 5c heme−NO complex as indicated by its EPR spectrum (Figure 8B). However, unlike sGC, the conversion from the 6c *Vc* H-NOX−NO complex to the 5c heme−NO complex is very slow. Moreover, no back conversion to Fe(II) *Vc* H-NOX was observed. In the presence of a higher NO concentration, a 2:1 ratio of NO to sGC leads to the formation of the 5c heme−NO complex with a Soret peak at 399 nm, presumably with NO coordinating to the heme on its proximal side.[5] In *Ns* H-NOX, however, a similar 5c heme−NO complex can be observed only in the presence of a high NO concentration. In the presence of a 2-fold excess of NO, an alternate 6c heme−NO complex forms in *Ns* H-NOX with a Soret peak at 414 nm.[14] In *Vc* H-NOX, in the presence of a NO concentration above the stoichiometric level, a 5c heme−NO complex forms readily with a Soret band at 398 nm. Similar to that for sGC, the rate of formation of the 5c heme−NO complex in the presence of an excess of NO is dependent on NO concentration, suggesting NO binds to the proximal side of heme.[8] However, the kinetics of formation of this 398 nm 5c heme−NO complex in *Vc* H-NOX is different from that in sGC. In sGC, the rate of formation of the 5c heme−NO complex is always linearly dependent on NO concentration, indicating that release of one NO molecule from the hypothetical quaternary complex intermediate is fast and not rate-limiting.[8] In *Vc* H-NOX, the rates of formation of the 5c heme−NO complex level off at high NO concentrations, suggesting that the formation of a quaternary complex intermediate (Scheme 1, C) becomes rate-limiting at high NO concentrations, with a limiting rate of 720 s^{-1} (Figure 6, inset). The rapid-freeze technique could be used to trap this transient intermediate, which may accumulate to a detectable level at very high NO concentrations.

As sGC and *Ns* H-NOX, *Vc* H-NOX does not show any appreciable association with O_2 to form an observable oxyferrous heme−O_2 complex at atmospheric pressure. On the other hand, the difference is observed for the subsequent autoxidation process. Ferrous sGC does not exhibit any noticeable autoxidation in the air, and Fe(II) *Ns* H-NOX was observed to autoxidize with a very slow rate of ~0.05 h^{-1}.[14] On the other hand, mixing O_2 with Fe(II) *Vc* H-NOX leads to a shift of the Soret peak within minutes (Figure 3). However, the transient oxyferrous *Vc* H-NOX−O_2 intermediate was not detected, presumably because of a large $k_{off}(O_2)$ constant outside the detection limit of our stopped-flow instrument. The observed spectral change is likely due to the autoxidation of Fe(II) *Vc* H-NOX as written in the following two equations:

$$\text{Fe(II) } Vc \text{ H-NOX} + O_2 \Leftrightarrow \text{Fe(II) } Vc \text{ H-NOX}{-}O_2 \quad (k_3,\ k_{-3}) \tag{III}$$

$$\text{Fe(II) } Vc \text{ H-NOX}{-}O_2 \Leftrightarrow \text{Fe(III) } Vc \text{ H-NOX} + O_2^{-\bullet} \quad (k_4,\ k_{-4}) \tag{IV}$$

The equilibrium of reaction III is biased toward the reactant side because of the large $K_D(O_2)$. Autoxidation as in reaction IV can be assumed to be irreversible (k_{-4} = 0). A Michaelis−Menten type kinetic relationship can therefore be written for the observed rate:

$$k_{obs} = (k_4[O_2])/(K_D(O_2) + [O_2])$$

Because the O_2 concentration used in the experiment is much lower than the projected $K_D(O_2)$, the previous equation can be simplified as

$$k_{obs} = [k_4/K_D(O_2)][O_2]$$

which explains the observed linear dependence of k_{obs} on $[O_2]$ (Figure 3B, inset). Overall, the rate constant of autoxidation of the Fe(II) *Vc* H-NOX−O_2 complex to Fe(III) *Vc* H-NOX can be estimated as k_4 = slope × $K_D(O_2)$ ~ 0.06 s^{-1} (Figure 3B). The autoxidation rate of Fe(II) *Vc* H-NOX is much faster than that of *Ns* H-NOX, 0.05 h^{-1}.[5,14] This relatively fast autoxidation also explains why $K_D(O_2)$ values for *Ns* H-NOX can be measured using a high-pressure cell and equilibrium titration, but not for *Vc* H-NOX.

Overall, the validity of the sliding scale rule hypothesis for the binding of gaseous ligands to heme sensor proteins is supported again by our detailed characterization of the binding of NO, CO, and O_2 to *Vc* H-NOX. The variations among the affinities of a particular gaseous ligand for sGC, *Ns* H-NOX, and *Vc* H-NOX and in the later phases of binding of NO and O_2 to these proteins are likely determined by the subtle environmental differences around their heme prosthetic groups.

Although crystallographic data are not yet available for *Vc* H-NOX, homology modeling against the structures of *Ns* H-NOX[9] or *Tt* H-NOX,[13] especially for the heme pocket, indicates that the key structural elements in binding the heme, His105 (proximal heme ligand, sGC numbering) and Tyr136, Ser138, and Arg140 (YXSXR motif),[7,44] are well-conserved. Tyr145, the H-bond donor that may contribute to preferential stabilization of O_2 in *Tt* H-NOX, is replaced with Ala145 in *Vc*

dx.doi.org/10.1021/bi401408x | *Biochemistry* 2013, 52, 9432−9446

H-NOX.[7,13] The exclusion of binding of O_2 to *Vc* H-NOX and the relatively fast autoxidation are only partially due to the lack of such an H-bond donor. Other factors, including the distal steric hindrance and proximal strain of the heme, likely play an even more important role in the increase in the log K_D values of all three gaseous ligands versus those for the heme model. Compared to that of *Ns* H-NOX, the distal steric hindrance seems to be much weaker for *Vc* H-NOX, with the distal bulky residue Trp74 in *Ns* H-NOX (or Phe74 in sGC) replaced by Leu74 in *Vc* H-NOX. Because the position of *Vc* H-NOX on the sliding scale plot (Figure 12) can almost be superimposed with of *Ns* H-NOX, the other factor(s), such as proximal constraints, may play a more dominant role in regulating the ligand affinity than distal steric hindrance in *Vc* H-NOX. Locating the structural component(s) that regulates the proximal constraints with crystallographic data for both wild-type and specific amino acid mutant(s) should provide incisive information about this issue and is our ongoing effort.

It has been proposed that the H-NOX domain in facultative aerobic bacteria, such as *Vc* H-NOX in *V. cholerae*, serves as a sensing domain and signals a shift to growth in a low-O_2 environment.[7] NO sensing may also play an important role in the pathology of *V. cholerae*. On the other hand, the infection of humans by *V. cholerae* causes massive production of inflammatory mediators, including reactive oxygen and reactive nitrogen species (ROS and RNS, respectively).[45−47] The induction of inducible nitric oxide synthase (iNOS) in this immunological response leads to a large amount of NO formation, serving as a bacterial killing agent in conjunction with the induction of myeloperoxidase biosynthesis to generate ROS.[45−47] iNOS itself can behave as a superoxide, hydrogen peroxide, or peroxynitrite synthase under uncoupled catalysis with a limited supply of either the L-arginine substrate or the cofactor tetrahydrobiopterin (unpublished results of V. Berka, W. Liu, G. Wu, and A.-L. Tsai and refs 48−50). Thus, these self-protective agents induced in the host will exert tremendous oxidative stress on the *V. cholerae* pathogen. Several key gene products for NO detoxification are induced in *V. cholerae*, including NO sensing and NO dioxygenase flavohemoglobins.[47] A certain counter stress mechanism is induced by ROS such as H_2O_2.[47] Although the functional partner(s) for *Vc* H-NOX has not been identified, dealing with the substantial stress of NO and ROS from host defense requires an efficient sensing mechanism for both NO and other ROS. In that respect, *Vc* H-NOX may behave like *Ns* H-NOX,[14] as a gaseous sensor and/or a redox sensor. Overall, the selective binding of ferrous *Vc* H-NOX to NO may provide to the pathogen a signaling pathway to respond to the environmental level of NO, which can be modulated by the immune response and iNOS activation of the host. This signaling pathway may therefore help the pathogen to survive the defense of the host and increase its virulence in the digestive tract where the oxygen content is fairly low. The information for the binding of ligands to ferric *Vc* H-NOX may also provide insights into the signaling pathway(s) for the survival of this pathogen under the possible redox states where *Vc* H-NOX exists in its ferric form. Therefore, our study of *Vc* H-NOX in both ferrous and ferric redox states should provide useful insights into the virulence of this human pathogen, especially the mechanism by which it deals with the host defense to sustain its colonization in the gastrointestinal tract.

■ ASSOCIATED CONTENT

Supporting Information

Absorption and MCD parameters of ferrous and ferric *Vc* H-NOX and their complexes (Table S1) and simulation of the binding of NO to the 6c *Vc* H-NOX−NO complex (Figure S1). This material is available free of charge via the Internet at http://pubs.acs.org.

■ AUTHOR INFORMATION

Corresponding Authors

*Hematology Division, Department of Internal Medicine, The University of Texas-Medical School at Houston, 6431 Fannin St., Houston, TX 77030. E-mail: gang.wu@uth.tmc.edu. Phone: (713) 500-6802. Fax: (713) 500-6812.

*E-mail: ah-lim.tsai@uth.tmc.edu. Phone: (713) 500-6771. Fax: (713) 500-6812.

Funding

This work was supported by National Institutes of Health Grant RO1 HL 095820 to A.-L.T.

Notes

The authors declare no competing financial interest.

■ ABBREVIATIONS

cGMP, cyclic guanosine monophosphate; CT, charge transfer; EPR, electron paramagnetic resonance; GTP, guanosine triphosphate; H-NOX, heme-nitric oxide and oxygen binding; iNOS, inducible nitric oxide synthase; Im, imidazole; LMCT, ligand-to-metal charge transfer; MCD, magnetic circular dichroism; Mb, myoglobin; metMb, metmyoglobin; NIR MCD, near-infrared MCD; *Ns* H-NOX, H-NOX protein found in *N. punctiforme*; sGC, soluble guanylyl cyclase; SONO, sensor of NO; *Tt* H-NOX, H-NOX protein found in *T. tengcongensis*; *Vc* H-NOX, H-NOX protein found in *V. cholerae*.

■ REFERENCES

(1) Jain, R., and Chan, M. K. (2003) Mechanisms of ligand discrimination by heme proteins. *J. Biol. Inorg. Chem. 8*, 1−11.

(2) Farhana, A., Saini, V., Kumar, A., Lancaster, J. R., Jr., and Steyn, A. J. (2012) Environmental heme-based sensor proteins: Implications for understanding bacterial pathogenesis. *Antioxid. Redox Signaling 17*, 1232−1245.

(3) Tsai, A.-L., Martin, E., Berka, V., and Olson, J. S. (2012) How do heme-protein sensors exclude oxygen? Lessons learned from cytochrome c′, *Nostoc puntiforme* heme nitric oxide/oxygen-binding domain, and soluble guanylyl cyclase. *Antioxid. Redox Signaling 17*, 1246−1263.

(4) Liebl, U., Lambry, J. C., and Vos, M. H. (2013) Primary processes in heme-based sensor proteins. *Biochim. Biophys. Acta 1834*, 1684−1692.

(5) Tsai, A.-L., Berka, V., Martin, E., and Olson, J. S. (2012) A "sliding scale rule" for selectivity among NO, CO, and O_2 by heme protein sensors. *Biochemistry 51*, 172−186.

(6) Derbyshire, E. R., and Marletta, M. A. (2012) Structure and regulation of soluble guanylate cyclase. *Annu. Rev. Biochem. 81*, 533−559.

(7) Boon, E. M., and Marletta, M. A. (2005) Ligand specificity of H-NOX domains: From sGC to bacterial NO sensors. *J. Inorg. Biochem. 99*, 892−902.

(8) Martin, E., Berka, V., Sharina, I., and Tsai, A.-L. (2012) Mechanism of binding of NO to soluble guanylyl cyclase: Implication for the second NO binding to the heme proximal site. *Biochemistry 51*, 2737−2746.

(9) Ma, X., Sayed, N., Beuve, A., and van den Akker, F. (2007) NO and CO differentially activate soluble guanylyl cyclase via a heme pivot-bend mechanism. *EMBO J. 26*, 578−588.
(10) Nioche, P., Berka, V., Vipond, J., Minton, N., Tsai, A. L., and Raman, C. S. (2004) Femtomolar sensitivity of a NO sensor from *Clostridium botulinum*. *Science 306*, 1550−1553.
(11) Boon, E. M., and Marletta, M. A. (2005) Ligand discrimination in soluble guanylate cyclase and the H-NOX family of heme sensor proteins. *Curr. Opin. Chem. Biol. 9*, 441−446.
(12) Karow, D. S., Pan, D., Tran, R., Pellicena, P., Presley, A., Mathies, R. A., and Marletta, M. A. (2004) Spectroscopic characterization of the soluble guanylate cyclase-like heme domains from *Vibrio cholerae* and *Thermoanaerobacter tengcongensis*. *Biochemistry 43*, 10203−10211.
(13) Pellicena, P., Karow, D. S., Boon, E. M., Marletta, M. A., and Kuriyan, J. (2004) Crystal structure of an oxygen-binding heme domain related to soluble guanylate cyclases. *Proc. Natl. Acad. Sci. U.S.A. 101*, 12854−12859.
(14) Tsai, A.-L., Berka, V., Martin, F., Ma, X., van den Akker, F., Fabian, M., and Olson, J. S. (2010) Is *Nostoc* H-NOX a NO sensor or redox switch? *Biochemistry 49*, 6587−6599.
(15) Tsai, A.-L., Berka, V., Chen, P. F., and Palmer, G. (1996) Characterization of endothelial nitric-oxide synthase and its reaction with ligand by electron paramagnetic resonance spectroscopy. *J. Biol. Chem. 271*, 32563−32571.
(16) Antonini, E., and Brunori, M. (1971) *Hemoglobin and Myoglobin in Their Reactions with Ligands*, Vol. *21*, North-Holland, Amsterdam.
(17) Pond, A. E., Roach, M. P., Thomas, M. R., Boxer, S. G., and Dawson, J. H. (2000) The H93G myoglobin cavity mutant as a versatile template for modeling heme proteins: Ferrous, ferric, and ferryl mixed-ligand complexes with imidazole in the cavity. *Inorg. Chem. 39*, 6061−6066.
(18) Olson, J. S. (1981) Stopped-flow, rapid mixing measurements of ligand binding to hemoglobin and red cells. *Methods Enzymol. 76*, 631−651.
(19) Kharitonov, V. G., Sharma, V. S., Magde, D., and Koesling, D. (1997) Kinetics of nitric oxide dissociation from five- and six-coordinate nitrosyl hemes and heme proteins, including soluble guanylate cyclase. *Biochemistry 36*, 6814−6818.
(20) Derbyshire, E. R., Gunn, A., Ibrahim, M., Spiro, T. G., Britt, R. D., and Marletta, M. A. (2008) Characterization of two different five-coordinate soluble guanylate cyclase ferrous-nitrosyl complexes. *Biochemistry 47*, 3892−3899.
(21) Gunn, A., Derbyshire, E. R., Marletta, M. A., and Britt, R. D. (2012) Conformationally distinct five-coordinate heme-NO complexes of soluble guanylate cyclase elucidated by multifrequency electron paramagnetic resonance (EPR). *Biochemistry 51*, 8384−8390.
(22) Galli, C., Innes, J. B., Hirsh, D. J., and Brudvig, G. W. (1996) Effects of dipole-dipole interactions on microwave progressive power saturation of radicals in proteins. *J. Magn. Reson., Ser. B 110*, 284−287.
(23) Maurus, R., Bogumil, R., Nguyen, N. T., Mauk, A. G., and Brayer, G. (1998) Structural and spectroscopic studies of azide complexes of horse heart myoglobin and the His-64→Thr variant. *Biochem. J. 332* (Part 1), 67−74.
(24) Hatano, M., and Nozawa, T. (1978) Magnetic circular dichroism approach to hemoprotein analyses. *Adv. Biophys. 11*, 95−149.
(25) Kajiyoshi, M., and Anan, F. K. (1975) Conformation of biological macromolecules. Circular dichroism and magnetic circular dichroism studies of metmyoglobin and its derivatives. *J. Biochem. 78*, 1087−1095.
(26) Tsai, A.-L., Kulmacz, R. J., Wang, J. S., Wang, Y., Van Wart, H. E., and Palmer, G. (1993) Heme coordination of prostaglandin H synthase. *J. Biol. Chem. 268*, 8554−8563.
(27) Cheesman, M. R., Greenwood, C., and Thomson, A. J. (1991) Magentic Circular Dichroism of Hemoproteins. In *Advances in Inorganic Chemistry* (Sykes, A. G., Ed.) pp 201−255, Academic Press, San Diego.
(28) Nozawa, T., Yamamoto, T., and Hatano, M. (1976) Infrared magnetic circular dichroism of myoglobin derivatives. *Biochim. Biophys. Acta 427*, 28−37.
(29) Rigby, S. E., Moore, G. R., Gray, J. C., Gadsby, P. M., George, S. J., and Thomson, A. J. (1988) N.m.r., e.p.r. and magnetic-c.d. studies of cytochrome f. Identity of the haem axial ligands. *Biochem. J. 256*, 571−577.
(30) Gadsby, P. M., Peterson, J., Foote, N., Greenwood, C., and Thomson, A. J. (1987) Identification of the ligand-exchange process in the alkaline transition of horse heart cytochrome c. *Biochem. J. 246*, 43−54.
(31) Dawson, J. H., and Dooley, D. M. (1989) Magnetic Circular Dichroism Spectroscopy of Iron Porphyrins and Heme Proteins. In *Iron Porphyrins, Part III* (Lever, A. B. P., and Gray, H. B., Eds.) VCH Publishers, Inc., New York.
(32) Blumberg, W. E., and Peisach, J. (1971) in *Probes and Structure and Function of Macromolecules and Membranes*, Vol. *2*, Academic Press, New York.
(33) Hori, H. (1971) Analysis of the principal g-tensors in single crystals of ferrimyoglobin complexes. *Biochim. Biophys. Acta 251*, 227−235.
(34) Palmer, G. (1985) The electron paramagnetic resonance of metalloproteins. *Biochem. Soc. Trans. 13*, 548−560.
(35) Gadsby, P. M. A., and Thomson, A. J. (1990) Assignment of the axial ligands of ferric ion in low-spin hemoproteins by near-infrared magnetic circular dichroism and electron paramagnetic resonance spectroscopy. *J. Am. Chem. Soc. 112*, 5003−5011.
(36) Dou, Y., Admiraal, S. J., Ikeda-Saito, M., Krzywda, S., Wilkinson, A. J., Li, T., Olson, J. S., Prince, R. C., Pickering, I. J., and George, G. N. (1995) Alteration of axial coordination by protein engineering in myoglobin. Bisimidazole ligation in the His64→Val/Val68→His double mutant. *J. Biol. Chem. 270*, 15993−16001.
(37) Schunemann, V., Trautwein, A. X., Illerhaus, J., and Haehnel, W. (1999) Mossbauer and electron paramagnetic resonance studies of the cytochrome bf complex. *Biochemistry 38*, 8981−8991.
(38) Friden, H., Cheesman, M. R., Hederstedt, L., Andersson, K. K., and Thomson, A. J. (1990) Low temperature EPR and MCD studies on cytochrome b-558 of the *Bacillus subtilis* succinate: Quinone oxidoreductase indicate bis-histidine coordination of the heme iron. *Biochim. Biophys. Acta 1041*, 207−215.
(39) Hederstedt, L., and Andersson, K. K. (1986) Electron-paramagnetic-resonance spectroscopy of *Bacillus subtilis* cytochrome b558 in *Escherichia coli* membranes and in succinate dehydrogenase complex from *Bacillus subtilis* membranes. *J. Bacteriol. 167*, 735−739.
(40) Carter, K. R., Tsai, A.-L., and Palmer, G. (1981) The coordination environment of mitochondrial cytochromes b. *FEBS Lett. 132*, 243−246.
(41) Tsai, A.-L., and Palmer, G. (1982) Purification and characterization of highly purified cytochrome b from complex III of Baker's yeast. *Biochim. Biophys. Acta 681*, 484−495.
(42) Wang, J. S., Tsai, A.-L., Heldt, J., Palmer, G., and Van Wart, H. E. (1992) Temperature- and pH-dependent changes in the coordination sphere of the heme c group in the model peroxidase N α-acetyl microperoxidase-8. *J. Biol. Chem. 267*, 15310−15318.
(43) Tsai, A.-L., Berka, V., Sharina, I., and Martin, E. (2011) Dynamic ligand exchange in soluble guanylyl cyclase (sGC): Implications for sGC regulation and desensitization. *J. Biol. Chem. 286*, 43182−43192.
(44) Iyer, L. M., Anantharaman, V., and Aravind, L. (2003) Ancient conserved domains shared by animal soluble guanylyl cyclases and bacterial signaling proteins. *BMC Genomics 4*, 5.
(45) Qadri, F., Raqib, R., Ahmed, F., Rahman, T., Wenneras, C., Das, S. K., Alam, N. H., Mathan, M. M., and Svennerholm, A. M. (2002) Increased levels of inflammatory mediators in children and adults infected with *Vibrio cholerae* O1 and O139. *Clin. Diagn. Lab. Immunol. 9*, 221−229.
(46) Janoff, E. N., Hayakawa, H., Taylor, D. N., Fasching, C. E., Kenner, J. R., Jaimes, E., and Raij, L. (1997) Nitric oxide production during *Vibrio cholerae* infection. *Am. J. Physiol. 273*, G1160−G1167.

(47) Stern, A. M., Hay, A. J., Liu, Z., Desland, F. A., Zhang, J., Zhong, Z., and Zhu, J. (2012) The NorR regulon is critical for *Vibrio cholerae* resistance to nitric oxide and sustained colonization of the intestines. *MBio 3*, e00013-12.
(48) Xia, Y., Dawson, V. L., Dawson, T. M., Snyder, S. H., and Zweier, J. L. (1996) Nitric oxide synthase generates superoxide and nitric oxide in arginine-depleted cells leading to peroxynitrite-mediated cellular injury. *Proc. Natl. Acad. Sci. U.S.A. 93*, 6770−6774.
(49) Xia, Y., Roman, L. J., Masters, B. S., and Zweier, J. L. (1998) Inducible nitric-oxide synthase generates superoxide from the reductase domain. *J. Biol. Chem. 273*, 22635−22639.
(50) Griffith, O. W., and Stuehr, D. J. (1995) Nitric oxide synthases: Properties and catalytic mechanism. *Annu. Rev. Physiol. 57*, 707−736.
(51) Gray, M. O., Karliner, J. S., and Mochly-Rosen, D. (1997) A selective ε-protein kinase C antagonist inhibits protection of cardiac myocytes from hypoxia-induced cell death. *J. Biol. Chem. 272*, 30945−30951.